Charge Dynamics Induced by Lithiation Heterogeneity in Silicon-Graphite Composite Anodes

Christopher Berhaut, Marta Mirolo, Diana Zapata Dominguez, Isaac Martens, Stéphanie Pouget, Nathalie Herlin-boime, Marion Chandesris, Samuel Tardif, Jakub Drnec, Sandrine Lyonnard

ADVANCED ENERGY MATERIALS
www.advenergymat.de

Charge Dynamics Induced by Lithiation Heterogeneity in Silicon-Graphite Composite Anodes

Christopher L. Berhaut, Marta Mirolo, Diana Zapata Dominguez, Isaac Martens, Stéphanie Pouget, Nathalie Herlin-Boime, Marion Chandesris, Samuel Tardif, Jakub Drnec, and Sandrine Lyonnard**

The reaction processes in Li-ion batteries can be highly heterogeneous at the electrode scale, leading to local deviations in the lithium content or local degradation phenomena. To access the distribution of lithiated phases throughout a high energy density silicon-graphite composite anode, correlative operando SAXS and WAXS tomography are applied. In-plane and out-of-plane inhomogeneities are resolved during cycling at moderate rates, as well as during relaxation steps performed at open circuit voltage at given states of charge. Lithium concentration gradients in the silicon phase are formed during cycling, with regions close to the current collector being less lithiated when charging. In relaxing conditions, the multi-phase and multi-scale heterogeneities vanish to equilibrate the chemical potential. In particular, Li-poor silicon regions pump lithium ions from both lithiated graphite and Li-rich silicon regions. This charge redistribution between active materials is governed by distinct potential homogenization throughout the electrode and hysteretic behaviors. Such intrinsic concentration gradients and out-of-equilibrium charge dynamics, which depend on electrode and cell state of charge, must be considered to model the durability of high capacity Li-ion batteries.

1. Introduction

In the search for high energy-density batteries to replace combustion engines in the automotive sector,[1] metals and metal-oxides such as silicon, germanium, or tin have been explored as anode materials.[2,3] Silicon in particular attracted a lot of attention due to its high theoretical specific capacity upon lithiation (>3500 mAh g^{-1}), ten times higher than that of graphite (372 mAh g^{-1}).[4] However, severe swelling during lithiation (≈300% for silicon vs ≈10% for graphite) hinders its use as anode material. The silicon volume variations lead to particle pulverization, increased active material surface area, continuous solid electrolyte interphase (SEI) growth, electrical disconnection, and thus the decay of electrochemical performance.[5–7]

To circumvent these issues, the nanostructuration of Si particles has been evaluated, and advanced designs were proposed using nanoparticles or nanowires, coatings, or even hierarchical structures inspired by egg yolk or pomegranate.[6,8–13] Currently, it is expected that high energy density electrodes will rely on composite systems, based on the combination of "robust" graphite and high-capacity Si, with the possible addition of stabilizing phase or dual-phase materials.[14–21] However, gaining knowledge on charging and capacity fading mechanisms remains a challenge to unlock large-scale applications of these materials.

To understand lithiation and aging mechanisms in detail, we need experimental techniques suited to probe both the nanostructured, usually amorphous, Si component and the crystalline graphite part in real-time and under real operation conditions.[3,22–24] Moreover, spatially resolving structural and morphological changes in the depth of the electrode and/or in 3D

C. L. Berhaut, S. Lyonnard
UGA, CEA, CNRS, IRIG, SyMMES
F-38000 Grenoble, France
E-mail: sandrine.lyonnard@cea.fr

The ORCID identification number(s) for the author(s) of this article can be found under https://doi.org/10.1002/aenm.202301874

DOI: 10.1002/aenm.202301874

M. Mirolo, I. Martens, J. Drnec
ESRF
71 Av. des Martyrs, F-38000 Grenoble, France
E-mail: drnec@esrf.fr

D. Z. Dominguez, S. Pouget, S. Tardif
UGA, CEA, IRIG, MEM
F-38000 Grenoble, France

N. Herlin-Boime
UPS, CEA, NIMBE
F-91191 Gif sur Yvette, France

M. Chandesris
UGA, CEA, Liten
F-38000 Grenoble, France

is crucial to understand how heterogeneities may evolve during cycling as well as their potential impact on battery performance. This is particularly important for thick industrial electrodes and fast charging conditions, where inhomogeneous (de-)lithiation processes unevenly distribute lithium across the material and may generate an increased amount of unavailable lithium localized in dead regions and thick SEI.[25–27]

The observation of silicon-graphite composite anode behavior is usually performed at one scale using a single-technique informing on either structure, chemistry, or morphology.[28–34] Yet, composite anodes are intrinsically complex hierarchical multiphase materials, where the interplay between reaction and aging mechanisms requires detailed information such as chemical-knowledge over time and over extended spatial dimensions, spanning from the atomic level up to device scale.[35,36] In this context, the combination of operando small and wide angle X-ray scattering (SAXS–WAXS) is enabling novel correlations, as SAXS is sensitive to changes at the nanoscale while WAXS probes the atomic order.[23,37]

Recently, the alloying process of silicon and the staging process of graphite were accessed in a single *operando* synchrotron SAXS/WAXS experiment performed on full cells in pouch geometry.[24] This study provided electrode-scale averaged information, for example, the amount of capacity contributed by each active material was extracted at any given state of charge, and the sequential (de-)lithiation mechanism was established. However, due to the transmission mode experiment, local effects such as lithiation gradients across the electrode thickness remained unresolved.

Herein, we report the operando SAXS/WAXS-computed tomography (CT)[29,38,39] study of a dual-phase high performance silicon-graphite composite anode in a custom-made half-cell. We identify heterogeneous lithiation processes during both cycling and relaxation steps, resolving the dynamics of lithium (re-)distribution between silicon and graphite phases across the depth of the electrode as well as in-plane. We observe that, on average, silicon is always receiving lithium from graphite during relaxations. However, we find distinct mechanisms in regions close to the separator against regions close to the current collector, due to the thermodynamics of surface chemical potential equilibrium, and hysteretic behavior of silicon. These findings highlight charge dynamics phenomena that must be accounted for to improve modeling of battery aging, not only under continuous current conditions but also in storage conditions or during realistic usage cycles.

2. Results

2.1. In-Plane/Through-Plane Structural Heterogeneities

The investigated anode is a dual-phase silicon-graphite composite that is rather porous and inhomogeneous in composition and morphology (Figure S1, Supporting Information). The silicon phase itself is a composite material made of a nanostructured amorphous Si phase mixed with crystalline $FeSi_2$ clusters.[22–24,40] The role of the iron disilicide in the composite is to buffer the Si expansion upon lithiation and improve the electronic conductivity.[14,20] While it is an active material (specific capacity of 60 mAh g^{-1}),[21] its relative capacity (2.5%) in the electrode is negligible compared to Si (68.5%) and graphite (29%), and it has even been shown to remain inactive when used with Si and ionic liquid electrolytes.[41] This material is studied in a custom-made half-cell battery by electrochemical cycling and SAXS/WAXS operando measurements. Details on the materials, cell assembly, design, and set-up are provided in the Supporting Information (Figure S2a–c, Supporting Information), together with typical real-time SAXS/WAXS data (Figure S2d,e, Supporting Information). The in-plane lithium content distribution is obtained from analyzing SAXS/WAXS-CT slices (T1 to T6) taken at three different depths in the electrode (*z*-positions close to the separator, in the middle of the anode, and close to current collector, i.e., z_{sep}, z_{mid}, and z_{cc}). These measurements are collected during relaxation steps started at given states-of-charge (SoC) over the course of the first cycle (**Figure 1**A) and second cycle (Figure 1B,C) charging steps. This is complemented by fast vertical 1D depth-scanning of the electrode during the relaxations at open circuit voltage (OCV, Figure 1E), to determine the dynamics of out-of-plane phase concentrations.

Both CT and 1D-scans are performed in WAXS and SAXS modes, allowing to quantify graphite and silicon lithiated structures concomitantly. Figure S3, Supporting Information, shows *z*-scan data (scan along electrode plane normal), evidencing the typical variations in WAXS and SAXS features on cycling. By analyzing the WAXS profiles, we can track the lithiation stage of graphite, looking at the peak intensities and positions between $q = 1.70$ Å^{-1} and $q = 1.90$ Å^{-1} and calculating the fraction of Li^+ in the graphite phase, x in $Li_x C_6$ (see Figure S4a, Supporting Information), labeled $x_{graphite}$.[23,28] The lithiation extent in Si phase, x in Li_xSi, labeled $x_{silicon}$, is evaluated by integrating the SAXS signal in the q region between 2×10^{-2} and 3×10^{-1} Å^{-1}, where the expansion of Si nanodomains gives rise to an extra-intensity and appearance of a characteristic correlation length related to the mean size of lithiated nanodomains (see Figure S4b, Supporting Information).[23,42] With a similar approach, different components of the cell can be identified (e.g., the PEEK body, as shown in Figure S5, Supporting Information).

The in-plane variations in time of both $x_{graphite}$ and $x_{silicon}$, measured in the middle of the composite anode, are reported in Figure 1C,D, respectively. Overall, it is seen that the lithiation trend follows the established sequential (de-)lithiation mechanisms.[25,28,43,44] During charge, graphite and Si lithiate at similar rates until full charge (T3), while upon discharge, graphite delithiates first (T4), followed by Si (T5). The second charging leads again to full lithiation of both graphite and Si (T6).

A more detailed analysis of the 2D colored maps in Figure 1C,D reveals in-plane heterogeneities that persist along the cycling sequence. They are found at all locations in the anode and within both active phases. Interestingly, some parts of the cell show significantly different graphite and silicon in-plane lithiation levels, even for a fully charged cell (T3). For instance, in the areas close to the cell walls, graphite is underlithiated (blue), while the Si phase is almost fully lithiated (red; see Figure S6, Supporting Information, for more details). Furthermore, we observe that the first and second full lithiations lead to a very similar in-plane distribution of lithiation inhomogeneities, which indicates that electrode configuration during manufacturing might lead to predetermined lithiation pathways. This is demonstrated

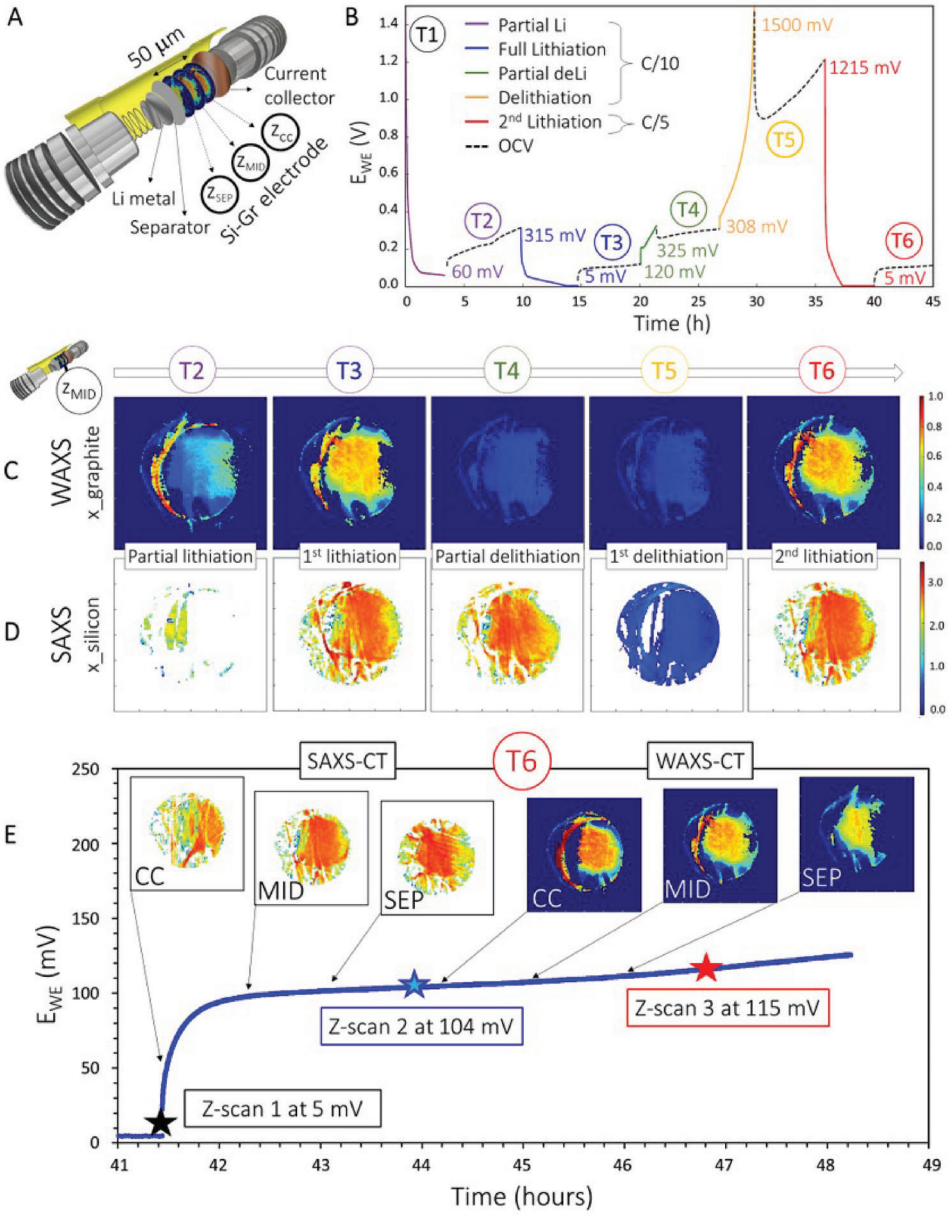

Figure 1. Visualizing structural heterogeneities. A) Operando cell for correlative SAXS/WAXS-CT performed in the composite anode at three positions: in the middle region (z_{MID}), close to current collector (z_{CC}), and close to separator (z_{SEP}). B) Electrochemical lithiation/delithiation sequence and relaxation steps at OCV (dashed lines) where SAXS/WAXS-CT sequences are performed (T1 to T6). C,D) Evolution of the 2D in-plane distribution of lithium content at z_{MID} during cell cycling. Pixels are colored from red-to-blue for high-to-low lithiation contents in graphite (C, x index in Li_xC_6 extracted from WAXS analysis) and silicon (D, x index in Li_x Si extracted from SAXS analysis). E) T6 data acquired at OCV. The potential relaxes from 5 to 115 mV during the 6 h time measurement where three SAXS slices (z_{CC}, z_{MID}, and z_{SEP}) are followed by three WAXS slices in identical positions. WAXS and SAXS 1D z-scans are performed to fast scan the depth of the electrode before, during, and after the CTs (black star, E_{we} = 5 mV; blue star, E_{we} = 104 mV; and red star, E_{we} = 115 mV).

by a high correlation in the internal structure of T3 and T6 slices, as shown in Figure S7, Supporting Information.

Further quantification of these large in-plane spatial (de-)lithiation variations is not trivial, because the various tomographic data are convoluted with time offsets, as seen on the typical measurement frame represented in Figure 1E, showing T6 as an example. The acquisition time for each tomography slice is about 1 h, causing a delay of ≈6 h between the first SAXS-CT acquired at position z_{CC} (E_{we} = 60 mV) and the last WAXS-CT acquired at position z_{SEP} (E_{we} = 112 mV). On the WAXS reconstructed slices, where the colors scale as $x_{graphite}$, we observe a decrease in lithiation content when measuring from the current collector (start CT time = 44.3 h, E_{we} = 105 mV) to the separator (start CT time = 46 h, E_{we} = 112 mV) positions. Contrarily, the lithiation of silicon observed in the SAXS slices shows an apparent global increase in lithium content in the in-plane maps

measured from the current collector to the separator. These observations point to a distinct behavior of the two active materials depending on their location inside the electrode. However, space-variations and time-variations arising from the large time-laps between the various datasets need to be decoupled. The differences observed in the WAXS-CT slices are not a direct indication of a z-dependent concentration gradient of Li^+ in graphite, but rather a time-dependent concentration, as shown in the next section.

2.2. Time-Resolved Lithium Concentration Dynamics

To further establish the dynamics of lithium content variations during cell relaxation, we analyze the fast 1D vertical scans. During the experiment, SAXS and WAXS z-scans are performed continuously along charge and discharge to monitor cell behavior. More importantly, they are also recorded during the relaxation steps, in between the sequences of tomography acquisitions. As indicated in Figure 1E, exemplary for T6 (SoC corresponding to T3 in Figure S7, Supporting Information), z-scans 1 to 3 are taken before the first WAXS-CT (black star, E_{we} = 5 mV), in between SAXS-CT and WAXS-CT (blue star, E_{we} = 104 mV) and at the end of the full relaxation period T6 (red star, E_{we} = 115 mV). This is very advantageous as it enables to check the impact of the potential drift on local phase heterogeneities.

Typical z-dependent WAXS and SAXS evolutions during the T6 relaxation step are shown in Figure S8, Supporting Information, while the full SAXS/WAXS intensity variations during the entire cycling sequence are displayed in Figure S9, Supporting Information. Note that we analyse z-values spanning from 15 µm (close to the separator) to 38 µm (close to the current collector), therefore covering most of the electrode but avoiding intensity artifacts in the WAXS and SAXS signal. It is clear that z-scan data acquired at the end of the first and second lithiations (T3 and T6) exhibit a reproducible and systematic trend, confirming the correlative analysis performed on the CT slices (Figure S7, Supporting Information). This is summarized in **Figure 2** for T6 and Figure S10, Supporting Information, for T3, where the time evolution of mean and depth-resolved lithiation contents of both graphite (gray) and silicon (red) phases are reported.

Our findings show that lithium ions get redistributed between the two active materials while the battery is kept at OCV after full lithiation. On average, in the electrode, lithium ions leave graphite to relocate into silicon domains (Figure 2A; Figure S10A, Supporting Information). The details of this mechanism are elucidated by analyzing the depth-resolved variations of $x_{graphite}$ and $x_{silicon}$, reported respectively in Figure 2B,C for T6 (see also Figure S10B,C, Supporting Information, for T3).

The lithium content in graphite across the electrode continuously decreases during the OCV step. As the lithiation is not fully completed during the second cycle (T6), the initial state is not fully lithiated (mean $x_{graphite} \approx 0.8$). At the end of the relaxation, the amount of lithium is decreased to ≈0.6, with no significant z-dependence (Figure 2B). In particular, $x_{graphite}$ ranges from 0.876 (z-scan 1) to 0.595 (z-scan 3) close to the separator (z = 15 µm), and from 0.85 to 0.6 close to the current collector (z = 38 µm). The flat profile along the z-direction is expected due to the graphite charge homogenization in the presence of silicon.[34] In contrast, the amount of lithium in silicon exhibits notable z-dependent features: $x_{silicon}$ increases when probing the region close to the current collector, while it decreases when probing regions close to the separator. This is directly visualized in Figure S9, Supporting Information, where the SAXS integrated intensities exhibit positive low-z and negative high-z trends during T3 and T6. We note that, in the initial state at 5 mV, silicon is, as expected, more lithiated close to the separator than close to the current collector.[25,43] Globally, the depth-dependent gradient observed in silicon tends to diminish with time, as a result of lithium redistribution to equilibrate the chemical potential through the electrode. Yet, a remaining non-monotonous shape is still observed at the end of the 6 h of relaxation, with a local maximum roughly in the center of the electrode, shifting toward the current collector with time (Figure 2C). This might be explained by the fact that z-scans probe only one region in the plane of the electrode (in the center of the cell and not on the edges). It cannot be excluded that, due to in-plane heterogeneities between the center and the edges (see Figure 1), faster paths for re-equilibration could be located out of the probed area, biasing the absolute levels of x in Li_xSi, but not the observed trends in dynamical behavior. Hence, we can conclude that the depleted region close to the current collector tends to relithiate during the relaxation to homogenize the concentration throughout the electrode, which goes at the expense of the initially highly lithiated region close to the separator.

All these evolutions are schematically summarized in Figure 2D where grayish and reddish squares indicate the amount of lithium in the graphite and in the silicon phases, respectively, as a function of the location in the electrode (from separator, top, to current collector, bottom). When the lithiation is stopped at 5 mV, graphite is homogeneous through the thickness of the electrode. It starts losing lithium during the subsequent relaxation step, without any lithium concentration gradients developing across the depth of the electrode. In contrast, silicon is either gaining or losing lithium, an effect that strongly depends on the localization in the anode.

2.3. Origin of Time-Space Heterogeneities

To elucidate the origin of the charge dynamics observed during relaxation, we compute the chemical potential µ of both graphite and silicon phases as a function of the lithiation index x, such that x = 1 corresponds to the most lithiated phases, LiC_6 and $Li_{3.75}Si$.[4] Both depth-averaged and depth-resolved situations are examined (**Figure 3**A–C,E–G). While $\mu_{graphite}$ only depends on the lithiation index (black line), $\mu_{silicon}$ also depends on the internal strain, σ, and therefore exhibits a strong hysteretic behavior.[45,46] Accordingly, several lithiation (red lines) and delithiation (orange lines) chemical potential curves can be considered depending on strain values ($\mu_{silicon} = f(x_{silicon}, \sigma)$, see Supporting Information and Figure S11, Supporting Information, for details). During relaxation, the material evolution has to bring the active particles of the composite anode to a common µ equilibrium value for the two phases, indicated by a green line in Figure 3B,F. We represent schematically the initial state of the anode by round symbols labeled i, located on the graphite and silicon curves at their corresponding initial lithium content values (Figure 3A,E). Similarly, we represent the final state f (Figure 3C,G), after transiting

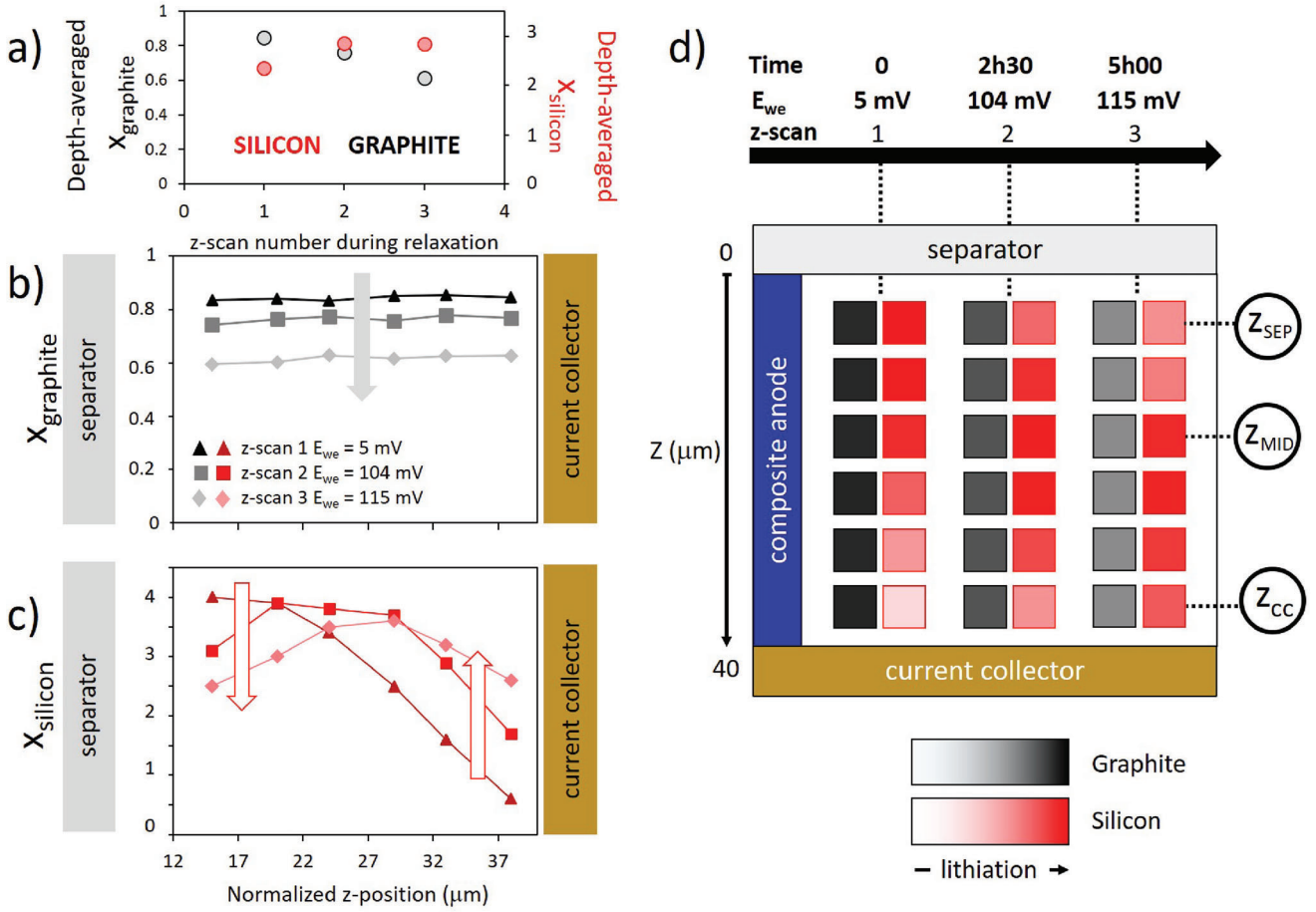

Figure 2. Lithium redistribution during a relaxation step (T6). A) Depth-averaged (mean) lithium content in graphite (gray) and silicon (red) obtained by performing fast WAXS/SAXS *z*-scans (1, 2, 3, at E_{we} = 5, 104, and 115 mV, respectively). B) Depth-resolved lithium content, $x_{graphite}$ and C) $x_{silicon}$, in the function of the *z*-position (close to the separator = 15 µm; close to the current collector = 38 µm) during the three *z*-scans as in (A). The gray arrow indicates the systematic decrease in lithium content in graphite, independent of the location, while the red arrows show that silicon gains lithium close to the current collector and loses lithium close to the separator. D) Schematic representation of the electrode dynamic evolution during relaxation. The gray (red) color bars indicate the amount of lithium in graphite (silicon). From left to right, time dynamics along *z*-scans 1 to 3. From top to bottom: Depth heterogeneities from the separator to the current collector.

through the intermediate state (Figure 3B,F) where the chemical potential of the two phases is equilibrating and, accordingly, points must move following the chemical potential curves, as indicated by arrows.

Let us first analyze the depth-averaged case, taking T6 data as input. The initial average lithiation content of each material of the composite electrode estimated from the WAXS and SAXS scans is $x = 0.8$ in graphite and $x = 0.6$ in silicon (see Figure 2B,C). These initial states (*i*) are indicated as black and red points corresponding to chemical potentials of 90 and 115 mV, respectively (Figure 3A). To reach the final experimental equilibrium potential (120 mV, Figure 1E), the two materials have only one way to evolve. The initial graphite point can only move leftward following the potential curve. Hence, graphite delithiates to reach its final state, point *f* at 120 mV (green line, $x = 0.6$ according to Figure 2A). During OCV, silicon experiences relaxation of the internal stress hence, the initial red silicon point *i* moves upward to one of the stress-relaxed lithiation curves (red dotted curves). To compensate for the graphite delithiation, silicon gets lithiated, following one of the relaxed lithiation curves toward a more lithiated final state f ($x = 0.8$ according to Figure 2A, filled red point). Note that this mechanism stays valid in all conditions, regardless of the exact initial location of the points on the curves. Therefore, the process of charge redistribution between these two active materials (also known as shuttle reaction) that we describe here is very general, as schematically represented in Figure 3D: On average, graphite always gives some lithium ions to silicon until both phases are equilibrated at the same potential.

The depth-resolved case is more complex, although it fundamentally obeys the same potential-driven equilibration mechanism. We have to consider not only the stress-relaxed lithiation curves (i.e., the potential evolution for silicon during relaxation, in which silicon gains in lithium content, depicted in red dotted lines in Figure 3B), but also the batch of silicon delithiation curves starting from various lithium contents (orange dotted curves in Figure 3F). Essentially, during OCV, highly lithiated silicon particles can start the delithiation process at a lower potential compared to the pseudo-equilibrium potential

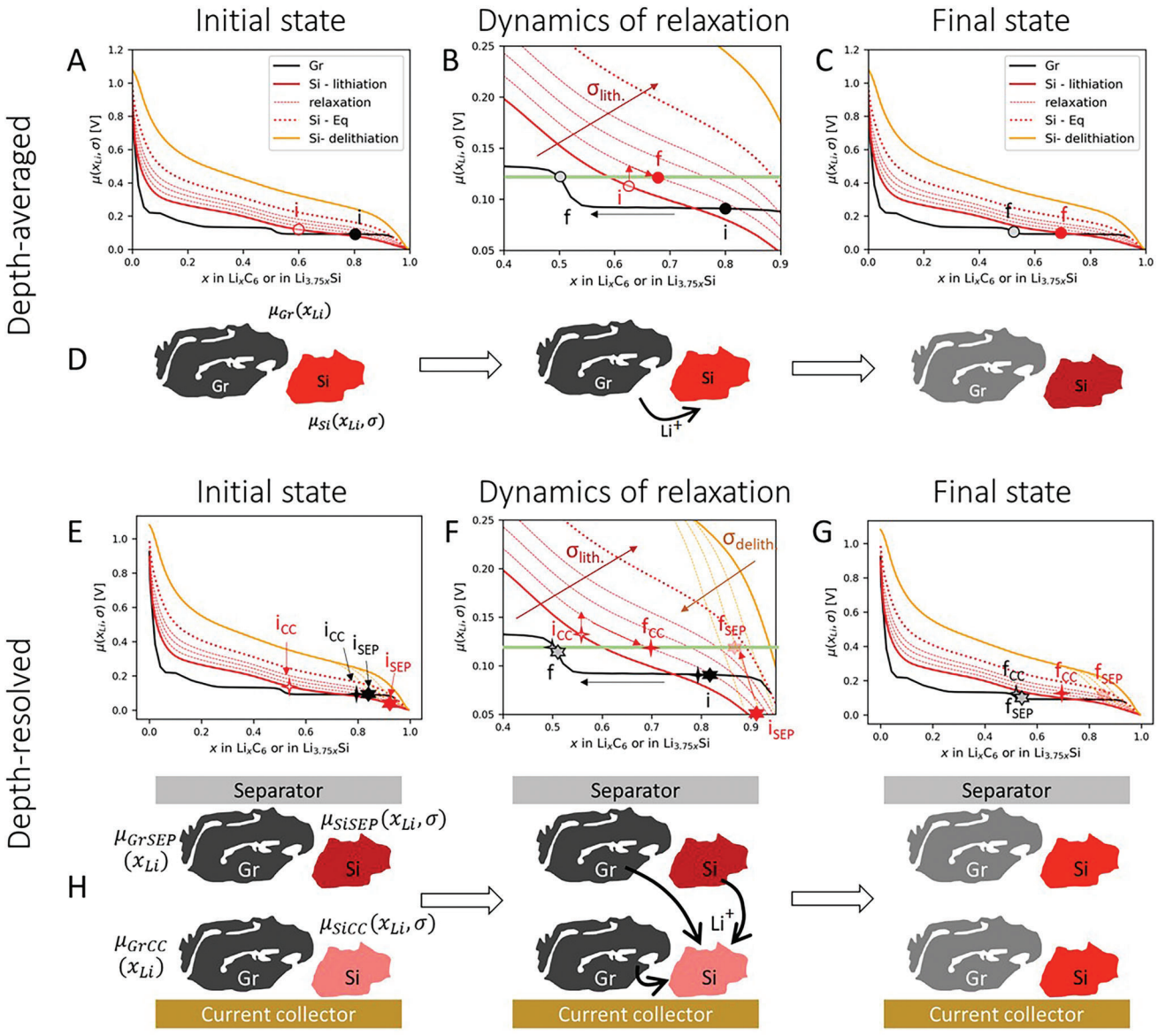

Figure 3. Mechanism of charge dynamics in silicon-graphite during relaxation (T6). Black line: Chemical potential of graphite. Red/orange lines: Chemical potential of silicon during lithiation and delithiation, shifted on decreasing stress (dotted red and orange lines) as highlighted with the dark red and dark orange arrows ($\sigma_{lith.}$ and $\sigma_{delith.}$, respectively). Filled symbols describe a higher lithiation state compared to empty ones (black points: graphite; red points: silicon). Initial states *i* (A,E); intermediate dynamics (B,F); final states *f* (C,G). A–C) Depth-averaged case: to equilibrate the system from the initial state ($x_{graphite} = 0.8$, $x_{silicon} = 0.6$) to the final state at 120 mV (green line in B), graphite can only get delithiated following the black potential curve, while silicon lithiates following the red arrows in the dotted curve due to the stress-relaxation at OCV. E–G) Depth-resolved case using two distinct initial situations: Close to separator (SEP, where silicon is initially more lithiated) and close to current collector (CC, where silicon is initially less lithiated). While close to the current collector graphite and silicon behave as in the depth-averaged case, close to the separator silicon starts to delithiate due to the lowering of the potential as the stress relaxes at OCV (dashed orange lines). Globally, as expressed in the schematic drawings (D,H), the equilibration of chemical potentials leads to graphite and lithium-rich silicon regions releasing lithium toward lithium-poor regions.

delithiation curve by following one of the orange dotted curves if its potential is lower than the one of the other particles. The initial space-heterogeneity in lithium content is represented by the two graphite star symbols (black, i_{CC}, and i_{SEP} at similar x values, close to 0.8 according to Figure 2B) and by the two silicon star symbols (red, i_{CC} at $x = 0.55$ and i_{SEP} at $x = 0.92$ according to Figure 2C). To reach the final equilibrium potential at 120 mV, graphite points move on the black potential curve to the left, as for the depth-averaged situation (moving from i_{CC}/i_{SEP} to f_{CC}/f_{SEP} states, $x = 0.8$ to $x = 0.5$). Silicon behaves differently depending on its location: silicon is initially much more lithiated close to the separator than close to the current collector ($i_{SEP} = 0.92$ and $i_{CC} = 0.55$). The silicon particles close to the current collector behave as in the average silicon case described above, following one relaxed lithiation curve until reaching a more lithiated state (red 4-branch-star, moving from $x = 0.55$ to $x = 0.72$). The

silicon particles sitting close to the separator (the six-branch red star symbol) follow one of the delithiation paths (dotted orange curve) and slightly move to the left of the graph to more delithiated states. Hence, silicon close to the separator slightly delithiates (from $x_{i,\,\mathrm{SEP}} = 0.92$ to $x_{f,\,\mathrm{SEP}} = 0.87$). Globally, the mechanism is represented in the sketch in Figure 3H, where we show how the lithium-depleted silicon region close to the current collector is lithiated from both graphite and lithium-rich silicon regions close to the separator.

This model allows us to account for the phenomena observed in the CT and vertical scans data, as well as the dynamics visualized in Figure 2. Based on the simple consideration that the silicon chemical potential depends both on lithium content and stress, we rationalize the dynamics of heterogeneities: i) observed between graphite and silicon particles; and ii) across the depth of the electrode during relaxation steps.

3. Conclusions

The (de-)lithiation mechanism in a composite electrode is a complex process due to the inherent nature of the electrode itself. Not only the Li^+ have different interactions with the materials (graphite and silicon, in the case described here), but its distribution might vary both in- and through-plane due to different kinetics and preferential pathways. To add more complexity, Li^+ flows not only when the current is applied, but a redistribution/equilibration is also observed during the relaxation of the cell potential at an open circuit. By employing a combination of fast vertical scans and WAXS/SAXS-CT we probe all these multiple effects and deconvolute the contribution of spatial and temporal dynamics to the overall (de-)lithiation process. Heterogeneities in the in-plane lithiation are observed at full charge due to the morphology of the electrode and the cell fabrication, in which the graphite particles do not fully lithiate close to the walls of the cell, while silicon is able to reach its fully lithiated state. Moreover, correlational analysis performed on CT slices acquired after the first and second lithiation shows that the electrode happens to be lithiated in the same areas, indicating a preferential lithiation pathway. When we look at the lithiation through the plane of the electrode, however, graphite and silicon show different behaviors. While graphite (de-)lithiates homogeneously across the electrode, silicon shows a lithium content gradient, with the silicon close to the separator being more lithiated than the silicon close to the current collector at the end of charging. Due to the spatial heterogeneities in the lithiation content of the graphite and silicon particles, there is a mismatch in chemical potential among the particles in the different locations of the depth of the electrode when the cell is left at open circuit potential. Hence, the charges equilibrate with time and we observe a partial and homogeneous delithiation of graphite and of the highly lithiated silicon particles close to the separator, in favor of the poorly lithiated silicon particles close to the current collector.

These effects combine and create intrinsic inhomogeneities not only during battery cycling but also during battery storage at OCV. The direct observation of charge dynamics and phase-to-phase redistribution during relaxation steps has several implications. First, it raises the question of experimental data fidelity when performing in situ measurements or operando characterization, especially when the time for data acquisition corresponds to some significant potential relaxation. Space-resolved mappings of properties might be convoluted with the time dynamics of the system and not represent a given SoC or specific situation of equilibrium but rather incorporate intricated processes that need to be identified and separated carefully. Second, the observed phenomena are not accounted for in cell-level models that aim at predicting battery aging by applying continuous current operation descriptions. Intermittent storage conditions, for example, periods of relaxation at OCV, are common in real applications. However, models usually do not incorporate the ingredients for describing these modes. Not integrating significant redistributions of charges may bias realistic aging prediction if usage cycles, including storage, are considered. Taking the graphite-silicon composite anode as an example, we see that, after pausing the charged battery, silicon uptakes lithium from graphite, therefore, it contains more lithium than any model would predict and may age more than anticipated. As the charge redistribution directly correlates to the chemical potentials of each component, we indicate that electrodes can be engineered to stay in the safe zone where each active material can be used with minimized charge transfers during storage.

Supporting Information

Supporting Information is available from the Wiley Online Library or from the author.

Acknowledgements

The authors acknowledge the financial support from the European Union's Horizon 2020 research and innovation program under grant agreement No. 685716 for the project "Silicon based Materials and New Processing Technologies for Improved Lithium-Ion Batteries (SiNTBAT)" and under grant agreement No. 875514 for the project "Ecologically and Economically Viable Production and Recycling of Lithium-Ion Batteries (ECO2LIB)." Roland Brunner from MCL is acknowledged for discussions on the materials properties and collaborations in the frame of the Sintbat project. Varta is acknowledged for providing the investigated material. The authors acknowledge the European Synchrotron Radiation Facility for the provision of synchrotron radiation facilities and also would like to thank the whole staff for assistance in using beamline ID31 (proposal number CH-5344). The data analysis has been performed in the frame of the Grenoble Battery Pilot Hub, proposal MA4929: "Multi-scale multi-techniques investigations of Li-ion batteries: towards a European Battery Hub."

Conflict of Interest

The authors declare no conflict of interest.

Author Contributions

C.L.B. and M.M. contributed equally to this work. S.L. developed the concept of the experiment in collaboration with C.L.B., S.T., S.P., and J.D. C.L.B. conceived the cell and performed the experiments, together with D.Z.D., S.P., S.T., N.H.-B., and S.L., helped by I.M. and J.D. C.L.B., S.P., S.T., S.L., M.M., and J.D. analyzed the data. M.C. performed the calculations and data interpretation was performed by M.M., S.T., M.C., J.D., and S.L. M.M., S.T., J.D., M.C., and S.L. wrote the manuscript with input from all authors. All authors revised the manuscript.

Data Availability Statement

The data that support the findings of this study are available from the corresponding author upon reasonable request.

Keywords

anodes, batteries, composite, graphite, operando, silicon

Received: June 15, 2023
Revised: August 27, 2023
Published online: October 3, 2023

[1] C. Hofer, G. Jäger, M. Füllsack, *J. Cleaner Prod.* **2018**, *183*, 1.
[2] L. Zhang, C. Zhu, S. Yu, D. Ge, H. Zhou, *J. Energy Chem.* **2022**, *66*, 260.
[3] D. Zapata Dominguez, C. L. Berhaut, A. Buzlukov, M. Bardet, P. Kumar, P.-H. Jouneau, A. Desrues, A. Soloy, C. Haon, N. Herlin-Boime, S. Tardif, S. Lyonnard, S. Pouget, *ACS Nano* **2022**, *16*, 9819.
[4] F. Ozanam, M. Rosso, *Mater. Sci. Eng., B* **2016**, *213*, 2.
[5] M. Yoshio, T. Tsumura, N. Dimov, *J. Power Sources* **2005**, *146*, 10.
[6] B. Wang, K. E. Aifantis, *Int. J. Mech. Sci.* **2022**, *215*, 106917.
[7] M. Schellenberger, R. Golnak, W. Quevedo Garzon, S. Risse, R. Seidel, *Mater. Today Adv.* **2022**, *14*, 100215.
[8] H. Wang, S.-H. Lu, X. Wang, S. Xia, H. B. Chew, *J. Phys. D: Appl. Phys.* **2021**, *55*, 063001.
[9] Y. Zhang, B. Wu, G. Mu, C. Ma, D. Mu, F. Wu, *J. Energy Chem.* **2022**, *64*, 615.
[10] Y. Yang, W. Yuan, W. Kang, Y. Ye, Q. Pan, X. Zhang, Y. Ke, C. Wang, Z. Qiu, Y. Tang, *Sustainable Energy Fuels* **2020**, *4*, 1577.
[11] G. Huang, J. Han, Z. Lu, D. Wei, H. Kashani, K. Watanabe, M. Chen, *ACS Nano* **2020**, *14*, 4374.
[12] D. H. S. Tan, Y.-T. Chen, H. Yang, W. Bao, B. Sreenarayanan, J.-M. Doux, W. Li, B. Lu, S.-Y. Ham, B. Sayahpour, J. Scharf, E. A. Wu, G. Deysher, H. E. Han, H. J. Hah, H. Jeong, J. B. Lee, Z. Chen, Y. S. Meng, *Science* **2021**, *373*, 1494.
[13] C. Keller, A. Desrues, S. Karuppiah, E. Martin, J. Alper, F. Boismain, C. Villevieille, N. Herlin-Boime, C. Haon, P. Chenevier, *Nanomaterials* **2021**, *11*, 307.
[14] H.-Y. Lee, S.-M. Lee, *J. Power Sources* **2002**, *112*, 649.
[15] Z. Du, R. A. Dunlap, M. N. Obrovac, *J. Electrochem. Soc.* **2014**, *161*, A1698.
[16] J. Asenbauer, T. Eisenmann, M. Kuenzel, A. Kazzazi, Z. Chen, D. Bresser, *Sustainable Energy Fuels* **2020**, *4*, 5387.
[17] A. Ghamlouche, M. Müller, F. Jeschull, J. Maibach, *J. Electrochem. Soc.* **2022**, *169*, 020541.
[18] J. Zhou, N. Lin, *Adv. Energy Sustainability Res.* **2022**, *3*, 2100198.
[19] S. Chae, S.-H. Choi, N. Kim, J. Sung, J. Cho, *Angew. Chem., Int. Ed.* **2019**, *59*, 110.
[20] Y. Domi, H. Usui, R. Takaishi, H. Sakaguchi, *ChemElectroChem* **2018**, *6*, 581.
[21] H. Usui, K. Nouno, Y. Takemoto, K. Nakada, A. Ishii, H. Sakaguchi, *J. Power Sources* **2014**, *268*, 848.
[22] T. Vorauer, P. Kumar, C. L. Berhaut, F. F. Chamasemani, P.-H. Jouneau, D. Aradilla, S. Tardif, S. Pouget, B. Fuchsbichler, L. Helfen, S. Atalay, W. D. Widanage, S. Koller, S. Lyonnard, R. Brunner, *Commun. Chem.* **2020**, *3*, 141.
[23] C. L. Berhaut, D. Zapata Dominguez, P. Kumar, P.-H. Jouneau, W. Porcher, D. Aradilla, S. Tardif, S. Pouget, S. Lyonnard, *ACS Nano* **2019**, *13*, 11538.
[24] C. L. Berhaut, D. Zapata Dominguez, D. Tomasi, C. Vincens, C. Haon, Y. Reynier, W. Porcher, N. Boudet, N. Blanc, G. A. Chahine, S. Tardif, S. Pouget, S. Lyonnard, *Energy Storage Mater.* **2020**, *29*, 190.
[25] E. Moyassari, L. Streck, N. Paul, M. Trunk, R. Neagu, C.-C. Chang, S.-C. Hou, B. Märkisch, R. Gilles, A. Jossen, *J. Electrochem. Soc.* **2021**, *168*, 020519.
[26] E. Radvanyi, E. D. Vito, W. Porcher, S. J. S. Larbi, *J. Anal. At. Spectrom.* **2014**, *29*, 1120.
[27] M. Weiss, R. Ruess, J. Kasnatscheew, Y. Levartovsky, N. R. Levy, P. Minnmann, L. Stolz, T. Waldmann, M. Wohlfahrt-Mehrens, D. Aurbach, M. Winter, Y. Ein-Eli, J. Janek, *Adv. Energy Mater.* **2021**, *11*, 2101126.
[28] K. P. C. Yao, J. S. Okasinski, K. Kalaga, J. D. Almer, D. P. Abraham, *Adv. Energy Mater.* **2019**, *9*, 1803380.
[29] D. P. Finegan, A. Vamvakeros, L. Cao, C. Tan, T. M. M. Heenan, S. R. Daemi, S. D. M. Jacques, A. M. Beale, M. Di Michiel, K. Smith, D. J. L. Brett, P. R. Shearing, C. Ban, *Nano Lett.* **2019**, *19*, 3811.
[30] P. Choi, B. S. Parimalam, L. Su, B. Reeja-Jayan, S. Litster, *ACS Appl. Energy Mater.* **2021**, *4*, 1657.
[31] S. Möller, H. Joo, M. Rasinski, M. Mann, E. Figgemeier, M. Finsterbusch, *Batteries* **2022**, *8*, 14.
[32] B. Key, R. Bhattacharyya, M. Morcrette, V. Seznéc, J.-M. Tarascon, C. P. Grey, *J. Am. Chem. Soc.* **2009**, *131*, 9239.
[33] B. Philippe, R. Dedryvère, J. Allouche, F. Lindgren, M. Gorgoi, H. Rensmo, D. Gonbeau, K. Edström, *Chem. Mater.* **2012**, *24*, 1107.
[34] J. Kim, M.-H. Kim, Y. Kim, M. S. Kim, A. Choi, K.-M. Jeong, H.-W. Lee, *Energy Storage Mater.* **2023**, *57*, 269.
[35] A. P. Black, A. Sorrentino, F. Fauth, I. Yousef, L. Simonelli, C. Frontera, A. Ponrouch, D. Tonti, M. R. Palacín, *Chem. Sci.* **2023**, *14*, 1641.
[36] A. Grant, C. O'Dwyer, *Appl. Phys. Rev.* **2023**, *10*, 011312.
[37] M. Povia, J. Sottmann, G. Portale, K. D. Knudsen, S. Margadonna, S. Sartori, *J. Phys. Chem. C: Nanomater. Interfaces* **2018**, *122*, 5917.
[38] S. R. Daemi, C. Tan, A. Vamvakeros, T. M. M. Heenan, D. P. Finegan, M. Di Michiel, A. M. Beale, J. Cookson, E. Petrucco, J. S. Weaving, S. Jacques, R. Jervis, D. J. L. Brett, P. R. Shearing, *Phys. Chem. Chem. Phys.* **2020**, *22*, 17814.
[39] I. Martens, A. Vamvakeros, N. Martinez, R. Chattot, J. Pusa, M. V. Blanco, E. A. Fisher, T. Asset, S. Escribano, F. Micoud, T. Starr, A. Coelho, V. Honkimäki, D. Bizzotto, D. P. Wilkinson, S. D. M. Jacques, F. Maillard, L. Dubau, S. Lyonnard, A. Morin, J. Drnec, *ACS Energy Lett.* **2021**, *6*, 2742.
[40] P. Kumar, C. L. Berhaut, D. Zapata Dominguez, E. De Vito, S. Tardif, S. Pouget, S. Lyonnard, P.-H. Jouneau, *Small* **2020**, *16*, e1906812.
[41] Y. Domi, H. Usui, Y. Shindo, S. Yodoya, H. Sato, K. Nishikawa, H. Sakaguchi, *Electrochemistry* **2020**, *88*, 548.
[42] S. Y. Lai, K. D. Knudsen, B. T. Sejersted, A. Ulvestad, J. P. Mæhlen, A. Y. Koposov, *ACS Appl. Energy Mater.* **2019**, *2*, 3220.
[43] P.-F. Lory, B. Mathieu, S. Genies, Y. Reynier, A. Boulineau, W. Hong, M. Chandesris, *J. Electrochem. Soc.* **2020**, *167*, 120506.
[44] C. Heubner, T. Liebmann, O. Lohrberg, S. Cangaz, S. Maletti, A. Michaelis, *Batteries & Supercaps* **2021**, *5*, e202100182.
[45] J. J. Brown, S.-H. Lee, J. Xiao, Z. Wu, *Phys. Status Solidi A* **2016**, *213*, 2156.
[46] M. Wang, H. Ye, *J. Power Sources* **2022**, *520*, 230803.